Tumor invasion as non-equilibrium phase separation

Wenying Kang[1*], Jacopo Ferruzzi[2*], Catalina-Paula Spatarelu[3], Yu Long Han[4], Yasha Sharma[1], Stephan A. Koehler[1], James P. Butler[1,5], Darren Roblyer[2], Muhammad H. Zaman[2,6], Ming Guo[4], Zi Chen[3], Adrian F. Pegoraro[7], Jeffrey J. Fredberg[1]

[1]Department of Environmental Science, Harvard T.H. Chan School of Public Health, Boston, MA, USA; [2]Department of Biomedical Engineering, Boston University, Boston, MA, USA; [3]Thayer School of Engineering, Dartmouth College, Hanover, NH, USA; [4]Department of Mechanical Engineering, Massachusetts Institute of Technology, Cambridge, MA, USA; [5]Department of Medicine, Brigham and Women's Hospital and Harvard Medical School, Boston, MA, USA; [6]Howard Hughes Medical Institute, Boston University, Boston, MA, USA; [7]Department of Physics, University of Ottawa, Ottawa, ON, CA.
*Contributed equally. **Correspondence should be addressed to J.J. Fredberg (jjf@harvard.edu).

TWO-SENTENCE SUMMARY: Using a multicellular spheroid embedded within an engineered three-dimensional matrix, we show here the potential for coexistence of solid-like, fluid-like, and gas-like phases of the cellular collective described by a jamming phase diagram. Depending upon cell type and matrix density, moreover, invasion into matrix from the tumor periphery can switch from a continuous cellular collective that flows like a fluid to discrete cells that scatter individually like a gas.

ASTRACT: The early malignant tumor invades surrounding extracellular matrix (ECM) in a manner that depends upon material properties of constituent cells and ECM. Biophysical mechanisms remain unclear, however. Using a multicellular spheroid embedded within an engineered three-dimensional matrix, we show here the potential for coexistence of solid-like, fluid-like, and gas-like phases of the cellular collective described by a jamming phase diagram. Depending upon cell type (MCF-10A *vs.* MDA-MB-231) and ECM density (1 to 4 mg/ml collagen), cancer cells within the spheroid display a variety of collective behaviors, including a non-migratory jammed phase and a migratory unjammed phase. At a critical collagen density, unjammed cancer cells at the spheroid periphery transition in an almost switch-like fashion between distinct modes of invasion. In the case of MDA-MB-231, for example, we find that when ECM density is 2 mg/ml or smaller single cells and cell clusters scatter from the spheroid periphery in the form of discrete gas-like particles, but when ECM density is 3 mg/ml or greater these cells flow collectively from the spheroid periphery in continuous fluid-like invasive branches. These findings suggest coexistence within the spheroid mass of multiple material phases of the cellular collective –solid-like, fluid-like, and gas-like– in a manner that is superficially similar to common inanimate multiphasic systems at thermodynamic equilibrium, but here arising in living cellular systems, all of which are displaced far from thermodynamic equilibrium. We conclude that non-equilibrium phase separation based upon jamming dynamics may provide a new physical picture to describe cellular migratory dynamics within and invasion from a tumor mass.

***Keywords*:** breast cancer, invasion, cell migration, unjamming, phase transition.

INTRODUCTION

Invasion of cancer cells from a primary tumor into surrounding tissue is a process wherein migration phenotypes can differ dramatically depending on the properties of the cells as well as those of their microenvironment [1]. It is well established that changes from one migratory phenotype to another depend upon a variety of factors that are cell specific, matrix specific, and interactive [1-3]. Current understanding of tumor dynamics begins with a core set of genetic alterations followed by driver mutations, evolution, competition, and resulting sub-clonal heterogeneity within the tumor mass [4, 5]. Moreover, cell invasion and escape from the primary tumor are often thought to require the epithelial-to-mesenchymal transition (EMT), which transforms the nominally non-migratory epithelial cell into the highly migratory mesenchymal cell [6, 7]. It is now known, moreover, that tumor cells can disseminate even at early stages of tumor development and then evolve at secondary sites in parallel with the primary tumor [8, 9].

From tumors of epithelial origin, cells often invade collectively, in multicellular strands, sheets, or clusters [2, 3, 10-12]. Mesenchymal clusters under confinement also display collective invasion despite their lack of cell-cell adhesions [13]. As regards the physics of such collective cellular migratory behavior and its role in tumor invasion, recent evidence implicates cell unjamming and the unjamming transition (UJT) [14-20]. For example, within a three-dimensional (3D) multicellular tumor, the core is suggested to approximate a jammed, solid-like phase in which cellular shapes tend to be rounded and cellular motions tend to be limited, intermittent, and caged by surrounding cells [15, 16, 21]. The periphery of the tumor, by contrast, tends toward a less jammed, more fluid-like phase in which cell shapes tend to become elongated and cellular motions tend to become larger, more cooperative, more persistent, and sometimes rotational [21]. Moreover, compared with cells in the spheroid core, cells at the spheroid periphery and invasive branches tend to become systematically softer, larger, longer and more dynamic [21]; these mechanical changes arise in part from supracellular fluid flow through gap junctions, suppression of which delays transition to an invasive phenotype. Increased levels of the small GTPase RAB5A and associated hyper-activation of the kinase ERK1/2 and phosphorylation of the actin nucleator WAVE2 have also been implicated [15].

Cell-matrix interactions are well studied, but an integrated physical mechanism that accounts for migratory dynamics of the cellular collective and its surrounding matrix is currently lacking. To bridge this gap, we first track cell shapes, packing, and migratory dynamics in the malignant multicellular micro-spheroid grown from a single non-malignant mammary epithelial cell [21, 22]. Within this system, we confirm spontaneous development of a solid-like jammed spheroid core and the gradual transition toward the periphery of an unjammed invasive front. We then go on to use the classical multicellular spheroid model of either non-malignant or post-metastatic epithelial cells embedded in a collagenous matrix [10, 11, 23]. When collagen density in this system is in the vicinity of 2.5 mg/ml, we find a critical transition that leads to striking multi-phasic differences in collective cellular behavior. Specifically, these differences are marked by the appearance at the spheroid periphery of either fluid-like collective invasion reminiscent of melting, or gas-like cell scattering reminiscent of sublimation. In the dynamics of the cellular collective, evidence therefore exists for solid-like,

fluid-like and gas-like phases. Finally, we describe a computational model of a tumor mass invading ECM. This model recapitulates coexistence of solid-like, fluid-like and gas-like phases of the cellular collective as governed by a jamming phase diagram. Together, these results suggest how heterogeneities within the tumor mass can become not only subclonal and regional but also –as a material– mechanical.

In the MCF-10A micro-spheroid, the core approaches a jammed, solid-like phase.

Structural signatures of unjamming. As a simplified model we start with the non-malignant MCF-10A epithelial cells embedded within an engineered interpenetrating network of Matrigel and Alginate [21, 22] (Methods). In these non-malignant cells, ECM stiffness by itself is sufficient to induce a malignant phenotype [22]. Here we varied the concentration of Alginate without changing the concentration of Matrigel, thus tuning the extracellular environment to a stiffness comparable to malignant breast cancer tissue. Within such matrices, MCF-10A cells spontaneously proliferate, form a micro-spheroid, and, over time, invade into the surrounding ECM (Figure 1A-B). For this reason, we examined evolution of the micro-spheroid at an early stage (days 3-5), when the spheroid is typically 30μm in radius and contains 46 ± 21 cells, and at a later stage (days 7-10), when asymmetric invasive protrusions extend up to 120μm from the spheroid center and the spheroid contains 169 ± 47 cells.

To quantify structural characteristics and packing of constituent cells, we identified nuclear locations from 3D confocal microscopy of cells transfected with green fluorescent protein tagged with nuclear localization signal (GFP-NLS). The spheroid boundary was identified from corresponding bright-field images (Figure 1A-B, insets). Using a bounded Voronoi approach based upon nuclear centroids, we then tessellated the space at each stage of spheroid growth and calculated for each cell the surface area, S, and the volume, V (Methods, Supplementary Figure 2).

Consistent with previous reports, cell volumes and nuclear volumes varied systematically throughout the spheroid and co-varied linearly (Supplementary Figure 3) [21, 24, 25]. In the late stage micro-spheroid, in particular, we found that cell volumes increased with radial position (Figure 1C) and cell number densities correspondingly decreased. These gradients have been observed previously and linked to supracellular fluid flows driven by frequently reported gradients of intra-tumor compressive stress [21]. Compressive stress within tumors is known to become large enough to collapse intra-tumor blood vessels and to increase the metastatic potential of cancer cells [26, 27].

We calculated for each cell a non-dimensional shape index (SI), given as the normalized surface area, $SI = S/V^{2/3}$, which can then be used as a structural signature of the degree of local unjamming and fluidization of the collective [19, 28-30], (Methods; Supplementary Figure 2). Cell shapes became progressively more elongated and more variable as the layer became progressively more unjammed [19, 29, 31]. The theory of cellular jamming suggests that as SI decreases towards a critical value of 5.4 the cellular collective approaches a jammed solid-like phase, while values of SI progressively greater than 5.4 signify collective phases that are progressively less jammed and more fluid-like [29]. This change is seen to occur in a continuous fashion, akin to jamming or glass transitions, as described below, with no discrete, structurally-distinct phase boundary

being evident. In the early stage micro-spheroid, SI was distributed homogenously with a mean of 6.01 ± 0.51 (Figure 1D), thereby suggestive of a relatively homogeneous fluid-like phase. In the late stage micro-spheroid, however, SI exhibited a clear positive radial gradient (Figure 1E). Near the spheroid center SI was 5.84 ± 0.32, which is smaller than that observed in the early stage, smaller micro-spheroid ($p<0.01$) and is thus indicative of a material phase in closer proximity to a jamming transition (Figure 1F). Near the spheroid periphery SI was 6.6 ± 0.79, which is greater than at the center ($p<0.01$) and is thus indicative of a material phase that is further removed from a jamming transition. At a late stage, therefore, the spheroid center tends to become more jammed and thus solid-like while the periphery tends to become more unjammed and thus fluid-like. We also determined for each cell in 3D the principal aspect ratios (AR_1, AR_2 and AR_3), which confirmed the radial trend towards unjamming suggested by the SI (Supplementary Figure 5).

In all cases the distributions of SI variation from cell-to-cell conformed to a *k-gamma* distribution (Supplementary Figure 6). In living systems, inert systems, and computational models, the *k-gamma* distribution has been thought to be yet another structural signature of granular systems approaching a jammed packing [19, 31, 32]. Using maximum likelihood estimation across all spheroid preparations, the average value of *k* was 10.2 ± 0.1, which is consistent with values previously reported in inert jammed 3D systems [32], where *k* is clustered around 12. We found little variation in *k* between stages of spheroid evolution (Supplementary Figure 6). This finding is reminiscent of those of Atia et al. in quasi two-dimensional (2D) cell layers [31], where over a wide range of cell types, *in vivo* and *in vitro*, different underlying pathological conditions, and even different species, *k* was found to fall into a narrow range between 1.9 and 2.5. It remains an open question as to why *k* seems to depend so strongly on dimensionality of the system (*i.e.*, 2D versus 3D) but relatively little on the nature of constituent particles.

Migratory signatures of unjamming. From image stacks acquired over 8 hours of micro-spheroid growth and cellular migration, we tracked for each cell the nuclear trajectory (Methods). In the early stage micro-spheroid there was no spatial gradient in cellular migratory speed, whereas in the late stage micro-spheroid the migratory speed increased systematically from the core to the periphery (Figure 1I). Cellular motions in the micro-spheroid core were small, sub-diffusive and thus showed evidence of caging (Supplementary Figure 4). In contrast, cellular motions in the micro-spheroid periphery were larger, super-diffusive, and thus showed no evidence of caging, consistent with reports from Valencia et al. [16]. These structural and migratory behaviors further support the interpretation that the center of the more mature spheroid tends to become more jammed and solid-like, whereas the periphery tends to become more unjammed and fluid-like [15, 16, 21].

In the MCF-10A macro-spheroid, the periphery invades as a locally unjammed fluid-like phase.

To assess the generality of these results, we examined invasion patterns and cell unjamming signatures in macro-spheroids embedded in matrices spanning a range of collagen densities. Compared to the micro-spheroids described above, these macro-spheroids were larger (extending to a radius of approximately 450μm from the spheroid center) and contained roughly 100-fold as many cells. To form a macro-spheroid we cultured MCF-10A cells on a low attachment substrate in presence of a small volume fraction of Matrigel and allowed

the cells to coalesce into a cluster over a period of 48 hours (Methods, Supplementary Figure 1). This cluster was then embedded into a self-assembling network of rat-tail collagen I fibrils at either low (2 mg/ml) or high (4 mg/ml) concentration. Using differential interference contrast (DIC) microscopy, these macro-spheroids were imaged continuously as constituent cells proliferated, remodeled the matrix, and initiated invasion. We then used optical clearing [33] and multiphoton microscopy [34] to obtain stacked images of DAPI-stained nuclei and used second harmonic generation (SHG) signal to obtain images of surrounding collagen (Figure 2A-B). Within the macro-spheroid, cell-free voids were frequently observed due to the presence of Matrigel (Supplementary Figure 1). In these cases, cell shape quantification was restricted to those cells that were either fully surrounded by neighboring cells and/or collagen (Methods, Supplementary Figure 2). To allow for comparison between radial distributions of cell shape and migratory dynamics, the latter was assessed using optical flow analysis [35] of DIC images (Methods) for the final 8-hour period (40-48 hours).

At the lower collagen density (2 mg/ml), the MCF-10A macro-spheroids invaded collectively in the form of continuous invasive protrusions and branches (Figure 2A). By contrast, at the higher collagen density (4 mg/ml), no invasion was observed (Figure 2B). Much as in the case of the micro-spheroids, in these macro-spheroids cell volumes were smaller near the core compared to the periphery (Figure 2C). Overall, however, the macro-spheroids exhibited smaller cell volumes than did the micro-spheroids, thereby suggestive of greater compressive stresses in macro-spheroids [21, 36]. Regardless of changes in collagen density, the spheroid core displayed SIs that were homogenous and small, thus indicating proximity to a solid-like jammed phase. By contrast, in low collagen density the collectively invading regions displayed increased and more variable SIs, indicating localized unjamming and progression towards a more fluid-like unjammed phase (Figure 2D-F). Migratory dynamics conformed to expectations from cell shapes. After correction for spheroid growth (Methods), migratory speed for cells in low density collagen increased mainly in those regions that had larger SIs and were collectively migrating within invasive branches (Figure 2G-H).

In the epithelial monolayer [17, 20, 37-40] and during 3D spheroid growth [41-43], previous studies have emphasized tissue unjamming and resultant fluidization through the action of cell proliferation. Nevertheless, for the following reasons proliferation seems an unlikely source of the regional unjamming reported here. In our model systems, changes in collagen density impacted neither spheroid growth nor cell proliferation (Supplementary Table 3). Instead, we observed larger and more variable cell shapes and faster dynamics restricted to sites where collective invasion occurred.

In MDA-MB-231 macro-spheroids, the invasive phenotype switches at a critical ECM density.

To generalize still further, we performed similar experiments using the post-metastatic cell line, MDA-MB-231 cells [44]. These cells are triple negative and claudin-low [45], form tumors that lead to poor prognosis [46], exhibit enriched expression in migration-relevant genes [47], and show strong invasive potential *in vitro* [48] and intermediate metastasis *in vivo* [49]. Because spheroid formation in these cells is mediated by integrin β1 adhesion with no cadherin involvement [50], these cells form macro-spheroids only in the presence of 2.5% Matrigel in the culture media [51] (Methods). For ease of comparison, both MCF-10A and MDA-MB-231 cells

were allowed to aggregate using Matrigel, which resulted in macro-spheroids of comparable size (Supplementary Figure 1). MDA-MB-231 spheroids were composed of approximately1000-5000 cells and often displayed a cell-free core occupied by ECM proteins (Figure 3; Supplementary Figure 1).

Restricting our structural analysis to the cells remaining within the continuous tumor mass and fully surrounded by neighboring cells and/or collagen, MDA-MB-231 cells had larger volumes with respect to MCF-10A cells after 48 hours of culture and invasion (Figures 2C and 3C), larger SIs, (Figures 2F and 3F) and higher motility regardless of collagen concentration (Figures 2I and 3I). Therefore, compared to MCF-10A spheroids, cells from post-metastatic MDA-MB-231 spheroids exist in a more motile fluid-like unjammed phase.

Within the MDA-MB-231 macro-spheroid in lower density collagen (2 mg/ml), cell volumes, SIs, and migratory dynamics were nearly homogenous (Figure 3C, 3F, and 3I). But to our surprise, in higher density collagen (4 mg/ml), cell volumes, SIs, and dynamics displayed a radially decreasing trend (Figure 3E-F), opposite to that observed in MCF-10A spheroids. Again, migratory dynamics changed in concert with changes in cell shapes. In lower density collagen, migratory speed was homogenously distributed within the tumor mass, while in higher density collagen, a consistent slow-down of migratory dynamics was observed within the invasive protrusions. We confirmed the presence of this proposed fluid-to-solid transition by monitoring temporal changes in cell shapes and migratory dynamics in time-lapse experiments of spheroid invasion (Supplementary Figure 7). Under conditions of greater confinement by the ECM, as the branch invaded into the matrix both SIs and cell speeds decreased.

We call special attention to the following observations. Using graded concentrations of collagen (1 to 4 mg/ml), we tracked over time the number of single MDA-MB-231 cells or cell clusters that had detached from the continuous primary spheroid mass, escaped that spheroid, and invaded in a gas-like fashion into ECM. The number of such single invading cells/clusters was found to be not only time-dependent but also critically dependent on collagen concentration (Figure 4A-C). On day 0 no cell escape was evident at any collagen concentration; immediately after embedded in collagen, all cells remained within the spheroid. On day 1 a modest level of cell escape became evident at lower collagen concentrations (1 and 2 mg/ml) but not at higher concentrations. On day 2 the number of detached invading cells became much larger and more highly sensitive to collagen concentration. By day 3, remarkably, the number of detached invading cells evolved into a striking biphasic switch-like dependence on collagen concentration. The critical collagen concentration demarking this step-like transition fell between 2 and 3 mg/ml.

To uncover structural and mechanical features of ECM that might underlie such criticality, we conducted high-resolution multiphoton microscopy imaging and confined compression testing at these graded collagen concentrations (Figure 4D-G). As collagen concentration increased, bulk compressive energy storage (quantifying the nonlinear material properties commonly referred to as stiffness, cf. Supplementary Methods) did not change whereas fiber density increased and both porosity and hydraulic permeability decreased (Figure 4D-G; Supplementary Figure 8).

Overall, these findings support the existence of a critical collagen density at which MDA-MB-231 cells at the spheroid periphery transition in an almost switch-like fashion between distinct modes of invasion. Under lower matrix confinement cells tend to invade individually as single cells or discrete cell clusters in a gas-like fashion. Under higher matrix confinement, however, these highly motile cells within invading protrusions progressively slow at the spheroid periphery and tend to rejam. For the invading cellular collective, these observations support the interpretation that high density collagen promotes steric hindrance and an associated confinement-induced jamming transition [13]. These events likely depend upon active remodeling of ECM by metalloproteases [52], cell generated traction forces [52-56], and the manner in which these tractions act to align collagen fibers [55]. These behaviors observed from micro- and macro-spheroids of MCF-10A and MDA-MB-231 cells are summarized in Table 1.

Mapping a hypothetical jamming phase diagram.

A two-dimensional hybrid computational model captures many of these striking behaviors. In the model, cortical tension and cell elasticity were incorporated much as in traditional vertex models [19, 30]. However, we modified those previous models through combination with an agent-based approach [57] that takes into account physical interaction between cells and the ECM, as well as the possibility of a gas-like phase. Each cell was assigned an elastic response to departures from a preferred area and a viscoelastic response to departures from a preferred perimeter (Supplementary Methods). In addition, each cell was endowed with self-propulsion of magnitude v_0, which acts as a vector with randomly generated polarity [31]. In departure from vertex based models, adjacent cells were given their own cell boundaries that moved along with the cell to which it belongs. ECM is represented as fixed and randomly distributed posts, the spatial density of which models changes in ECM density.

We varied ECM density and cellular propulsion while maintaining all other parameters fixed (Supplementary Table 1). ECM density was chosen as the matrix-dependent control variable based on our experimental results (Figure 4), and cellular propulsion was chosen as the corresponding cell-dependent control variable based on previous models of epithelial unjamming demonstrating its critical role in jamming [30]. The choice of cellular propulsion was further supported by the observation that MDA-MB-231 cells are more motile with respect to MCF-10A cells (Figures 2 and 3). We classified the material state of the modeled spheroid based on the end position of peripheral cells, and found that this simple model maps out a jamming phase diagram in which solid-like, fluid-like, and gas-like phases are seen to co-exist (Figure 5; Supplementary Table 2).

When v_0 is small the cellular collective shows solid-like behavior with little migration or invasion, and thus resembles the MCF-10A macro-spheroid in high density collagen (Figure 5, region A). When v_0 is progressively increased while keeping collagen density fixed and small, single cells and cell clusters detach from the collective and thus mimic gas-like dispersion as observed in MDA-MB-231 spheroids in low density collagen (Figure 5, region C). When collagen density is increased while v_0 is held fixed, this gas-like dispersion is suppressed in favor of fluid-like collective cellular flows that protrude in branches from the continuous tumor mass (Figure 5, region B). Therefore, collagen density and cell propulsion are then seen as control variables

that tune the material phase and the mode of invasion. This computational model and the resulting jamming phase diagram thus provide a useful guide for thought and, potentially, a unifying mechanistic interpretation.

Discussion

Within the experimental model systems employed here, transitions in tumor cell morphology, packing and overall migratory dynamics bear a striking resemblance to those observed in jammed packings typical of many inanimate inert collective systems [32]. We suggest, therefore, that tumor cells, their interactions with one another, and their interactions with the ECM, lead to collective cellular migration and escape governed by coexisting material phases (solid-like, fluid-like, gas-like) and an overriding jamming phase diagram. A plausible example of one such phase diagram is sketched in Figure 5. This new physical picture provides mechanistic insights concerning how specific physical factors affect the behavior of tumor cells *en masse* and their invasive behavior in the early tumor. Based upon such an integrated conceptual framework, we suggest, further, that innumerable physical features characterizing tumor cells, their interactions with one-another, and their interactions with the ECM may map into a small set of 'effective' thermodynamic variables, such as an effective temperature (Box 1) and an effective confinement pressure (Box 2).

In that connection, the distinction between a jamming transition and a glass transition is clear but subtle [58]. The glass transition captures the conversion between fluid-like and solid-like phases as arises from the competition amongst cellular crowding, adhesion, contraction and agitation [30]. The jamming transition, by contrast, is framed purely as a geometric transition between fluid-like and solid-like phases regardless of dynamics [59]. But mainly because it can be more easily grasped, much of the recent literature on collective cellular migration frames observations in the context of the jamming, unjamming, and the unjamming transition (UJT). But within either frame of reference, the material phases described and the transitions between them are not to be confused with first order or second order transitions as occur in systems close to thermodynamic equilibrium. As opposed to precisely defined thermodynamic states, for example, the material phase of a cellular collective must be defined via functional terms – cellular shapes, collective fluidity, migratory dynamics, and migratory cooperativity. Moreover, in such systems the transition between solid-like and fluid-like behavior is continuous and smeared –both in space and in time– as opposed to binary and sharp, thus precluding identification of the precise position of a boundary between phases.

As used here, the phrase 'coexistence' of material phases has two distinct but interrelated connotations. The first suggests that a homogenous cellular collective can attain simultaneously, and at every position, a local state in close proximity to a jamming phase boundary. For example, each line depicted in Figure 5 represents such a phase boundary, one each for coexistence between solid-fluid, fluid-gas, and solid-gas phases, and, near the triple point, coexistence between solid-fluid-gas (Figure 5). As suggested previously [60], in the vicinity of such a phase boundary, seemingly modest changes of cellular or ECM properties may have the potential to precipitate striking global changes of material phase and invasion phenotype. The second connotation suggests that radial non-uniformities in local conditions can cause the cellular collective to express macroscopic regional differences, such as a solid-like core coexistent in the same tumor with a fluid-like

invasive branch. Because these phases appear to be controlled by jamming dynamics and resemble a glass transition, there is no distinct spatial boundary between these phases. Just as there is no latent heat and no structural signature of melting for inert materials approaching the glass melting point, so too there is no sharp transition in cellular SI or migration speed in the late-stage MCF-10A micro-spheroid.

Despite the lack of a distinct phase boundary within the micro-spheroid, from morphological and functional viewpoints the core and periphery of larger spheroids clearly exist in different states. Compared with cells nearer the core of the spheroid, cells at the periphery tend to be systematically more elongated, more variable in shape, and more migratory (Figures 1-4). And in the context of active force fluctuations and associate metabolism, they are more dynamic [21, 61]. Together, this constellation of structural, migratory, mechanical, and metabolic factors is consistent with an effective temperature, T_{eff}, that is locally elevated at the tumor periphery compared with the core. When appropriately interpreted, such a physical picture would help to explain, and perhaps to generalize, the x-axis of the hypothesized jamming coexistence phase diagram (Figure 5; Box 1). As regards the y-axis of the hypothesized phase diagram, it is well established that mechanical stress and interstitial fluid stress within the spheroid core are compressive, and that cellular and nuclear volumes are reduced, as if under compression [21, 26, 62]. Furthermore, osmotic pressure decreases cellular volume, increases cell stiffness and thereby decreases invasiveness of peripheral cells [21]. But it remains unclear how neighboring cells, ECM, or interstitial fluid stress, or osmotic stress might be related to the hypothesized confinement pressure, P_{conf}. Such connections, if they could be established, would help to explain, and perhaps to generalize, the y-axis of the hypothesized jamming coexistence phase diagram (Figure 5; Box 2).

It remains unclear how a generalized UJT process is related to a more canonical metastatic pathway such as the epithelial-to-mesenchymal transition (EMT). A central role of the EMT in tumor cell motility, invasiveness, and metastasis, is well established but has recently become a point of contention [63, 64]. Our results suggest that relative to EMT, the UJT is a complementary route for establishment of cell motility and invasiveness. Indeed, in at least one system the UJT and collective migration are known to occur in the absence of EMT [65]. In systems tested here, MDA-MB-231 cells lack E-cadherin and are therefore mesenchymal-like. However, when embedded in high density collagen, these cells undergo confinement-induced jamming while still retaining fluid-like collective invasive behavior (Figure 3; [13]), thus indicating that jamming and UJT remain influential in collective behavior. Establishing the extent to which the UJT may be complementary to or, potentially, may subsume EMT in directing collective cellular motion seems a necessary step for fuller understanding cancer progression.

As regards different model systems of the early tumor *in vitro* as well as breast tumors in native environments in *vivo*, it is to be expected that variation in cancer cell types or their origin, receptor complement, ECM composition, and immune and stromal cell complement will lead to quantitative or even qualitative departures from the behaviors reported here. Nevertheless, the concepts of UJT and non-equilibrium phase separation may offer a unifying physical framework that is sufficiently general to provide

novel insights and explanatory power. In any event, simplified model systems such as the ones studied here demonstrate that collective cellular migration, invasion and escape from a cellular mass involve biophysical processes far richer than previously anticipated. We have suggested how details of cell and ECM properties of cell collectives can be reduced to a set of 'effective' thermodynamic variables and mapped onto a phase diagram that governs the invasion pattern and material phase. But how the local material phase of the cellular collective and its mechanical properties might impact the emergence of driver mutations remains unknown. Specifically, deformation of the cell and its nucleus associated with migration within a highly confining microenvironment is known to cause loss of nuclear envelope integrity, herniation of chromatin across the nuclear envelope and DNA damage [66], but the impact of cell and nuclear elongation in connection with unjamming remains unstudied. Conversely, how driver mutations and resulting subclonal heterogeneities might impact the local material phase is also unclear. When such interactions become appreciable, tumor dynamics would then be seen to be a multifaceted problem in mechanogenetics [67].

Acknowledgments

This work was funded by the National Cancer Institute (grant number U01CA202123); the National Heart Lung and Blood Institute (P01HL120839). Z.C. acknowledges the Branco Weiss - Society in Science Fellowship, administered by ETH Zürich; the Dartmouth University startup fund. C.S. acknowledges the Dartmouth University Ph.D. Innovation Fellowship at Thayer School of Engineering. M.G. acknowledges the Sloan Research Fellowship. A.F.P. acknowledges NSERC Discovery and NSERC CRD grants to A Stolow, the NRC-uOttawa Joint Centre for Extreme Photonics, and the Max-Planck-University of Ottawa Centre for Extreme and Quantum Photonics. D.R. acknowledges the Department of Defense (DoD grant W81XWH-15-1-0070). We also gratefully acknowledge Elizabeth Bartolak-Suki (Boston University) for expert assistance with spheroid histology, and Lauren O'Keeffe (Cornell University) for assistance with spheroid embedding and cell counting.

Author Contributions

W.K., J.F., J.J.F designed the study; J.F., Y.L.H, D.R. performed experiments; C.S. and Z.C. performed simulations; W.K., J.F., Y.S., S.K. analyzed data; W.K., J.F., A.F.P., J.P.B., J.J.F. interpreted data; W.K, J.F, A.F.P, J.J.F. wrote the manuscript; W.K., J.F., C.S., Y.L.H., J.P.B., J.B., M.G., Z.C., M.Z., A.F.P, J.J.F. reviewed and edited the manuscript. J.J.F oversaw the project.

METHODS

Cell lines and culture media. Non-tumorigenic MCF-10A and metastatic MDA-MB-231 breast epithelial cell lines were purchased from American Type Cell Culture Collection (ATCC) and cultured using standardized media and conditions [21, 52]. MCF-10A cells were cultured in DMEM/F-12 (ThermoFisher, No. 11330032) supplemented with 5% horse serum (Invitrogen, No. 16050122), 20 ng/ml EGF (Peprotech, AF10015; ThermoFisher, No. 10605HNAE), 0.5 mg/ml hydrocortisone (Sigma-Aldrich, No. H0888), 100 ng/ml cholera toxin (Sigma-Aldrich, C8052), 10 µg/ml insulin (Sigma-Aldrich, No. I1882). MDA-MB-231 cells were culture in DMEM (Corning, No. 10013CV), supplemented with 10% fetal bovine serum (ATCC, No. 302020). Both media recipes contained 1% penicillin/streptomycin (ATCC, No. 302300; ThermoFisher, No. 15140122). Cells were maintained at 37°C and 5% CO_2 in a cell culture incubator.

Spheroid formation. Two distinct protocols were used to generate the micro- and macro-spheroid models used in this study. First, micro-spheroids were formed by trypsinizing and embedding MCF-10A cells within an interpenetrating network (IPN) consisting of 5 mg/ml Alginate (FMC Biopolymer) and 4 mg/ml Matrigel (Corning, No. 354234) as previously shown [21, 22]. Cells were mixed with the gel precursor solution, which was allowed to gel inside an incubator before adding culture media. The shear modulus of the double network can be tuned via calcium cross-linking and was herein set to 300 Pa to reproduce the stiffness of a malignant breast tissue [22]. Within the IPN, cells proliferated to form micro-spheroids that began invading into the gel after approximately 7 to 10 days in culture. Second, MCF-10A and MDA-MB-231 macro-spheroids were generated by seeding approximately 10^3 cells in each of the 96 wells of an ultra-low attachment plate (Corning, No. 07201680) and allowed to form for 48 hours in presence of 2.5% v/v Matrigel. We verified that addition of a small volume fraction of Matrigel allows formation of MDA-MB-231 spheroids, which would otherwise form only loose aggregates (Supplementary Figure 1, and [51]). MCF-10A spheroids were formed under the same conditions to ensure consistency. Once formed, individual spheroids surrounded by a small volume of media were transferred in microwells (10 mm in diameter) inside of glass bottom 6-well plates (MatTek, No. P06G-0-10-F) by pipetting 5 µl drops on each of the coverslips. Each spheroid was covered by 145 µl of ice-cold, rat-tail collagen I solution to achieve a total volume of 150 µl and a specific collagen concentration in each microwell. Collagen solutions were prepared by mixing acid-solubilized collagen I (Corning, No. 354249) with equal volumes of a neutralizing solution (100 mM HEPES buffer in 2x PBS) [68, 69]. The desired collagen concentration was reached by adding adequate volumes of 1x PBS. Collagen solutions at different concentrations (1, 2, 3, and 4 mg/ml) polymerized for 1 hour at 37°C. The cell culture plates were rotated every minute for the first 10 minutes of polymerization to guarantee full embedding of the spheroid within the 3D collagen matrix. Finally, 2 ml of culture media was added and the 3D organotypic culture was placed inside the incubator for a variable amount of time. Media was refreshed every two days.

Measurement of micro-spheroid dynamics. MCF-10A cells were stably transfected with GFP-linked nuclear localization (NLS-GFP). To track the movement of individual cells, micro-spheroids at early (3-5 days) and late (7-10 days) stage of growth were imaged every 10 minutes for 12 hours in a customized incubator (37°C, 5% CO_2, and 95% humidity) on a confocal microscope (Leica, TCL SP8), with acquisition of fluorescent and bright-field image z-stacks (Figure 1A-B). Analysis of cell migratory dynamics was done based on the obtained image z-stacks according to the procedures outlined below, implemented in custom MATLAB programs (cf. *nuclei identification*). Using an adaptation of previously published methods [70], the 3D coordinates of each cell nucleus were identified at each frame based on maximum intensities from the fluorescent images. Cell trajectories were constructed through minimization of overall nuclear displacements between sequential frames. Cell positions from each time point were aligned to the micro-spheroid geometric center at the initial time point t_0 to account for any translational motion that may have occurred due to stage drift. To separate the contribution of Coherent Angular Motion (CAM) of the early micro-spheroid from migratory dynamics due to individual cell rearrangement, we solved for the rigid rotational transformation ω that best reproduced the changes occurred in cell nuclei positions ($p(x,t)$) between z-stacks during the time interval Δt. ω is defined as the rotation that minimized the metric $d(\omega|t) = \|p(x,t+\Delta t) - R(\omega\Delta t)p(x,t)\|$. This rigid rotational motion from CAM is removed from cell trajectories before further calculations of cellular dynamics. Root mean squared (RMS) speeds for each cell were calculated using the instantaneous velocity vectors. Mean squared displacements (MSD) were computed as a function of time interval, $MSD(\Delta t) = \langle|p(x,t+\Delta\mathrm{t}) - p(x,t)|^2\rangle$. Here, $\langle\dots\rangle$ denotes an average over time, with overlap in time intervals.

Measurement of macro-spheroid dynamics. A customized spinning disk confocal setup equipped with an environmental chamber (37°C, 5% CO_2, 80% relative humidity) was used for imaging spheroid invasion

in collagen. For each spheroid within a 6-well plate, differential interference contrast (DIC) images were collected every 10 minutes for 48 hours as 3×3 tiled, 200 µm z-stacks. A 10x air objective was used to image large areas (1450.3 × 1450.3 µm) with a resolution of 1.126 µm/pixel. Automated stitching based on global optimization of the 3D stacks [71] was carried out using ImageJ (v. 1.52g, National Institute of Health, Bethesda, MD). Minimum intensity projections of the stitched DIC time-lapse data were used to visualize the 3D data sets as 2D movies while maximizing the image contrast (dark spheroid/cells on a light background). These DIC movies were imported in MATLAB (R2019a, Mathworks, Natick, MA), where images from individual time frames were down-sampled by 50% (2.252 µm/pixel) to optimize the processing speed. De-jittering of movies was achieved using an optimized image registration algorithm [72]. Temporal evolution of the projected macro-spheroid area was segmented using Otsu's method [73], where the optimal threshold was calculated over three consecutive frames to smooth changes in area between frames. The resulting binary mask allowed us to separate between the spheroid interior (i.e., main spheroid) and exterior (i.e., single cells migrating in collagen, if any). To estimate the direction and speed of collective migration within the macro-spheroid, we employed Farneback's optical flow method [74] using the MATLAB function *estimateFlow* with the option *opticalFlowFarneback* and a Gaussian filter size of 8 pixels while keeping all the other parameters to their default values. At each frame, velocity vectors are obtained for seed points spaced 2 µm apart that are inside the spheroid mask. To account for the effect of collective motion from spheroid growth on migratory dynamics, we estimated spheroid radial growth rate through tracking of change in spheroid mask area over time. This velocity was interpolated for each seed depending on its location within the spheroid, and were removed from the velocity vectors before RMS speed calculations Single cells lying outside the spheroid mask were detected based on local intensity minima at each frame, and tracks constructed by minimizing displacements of cells between consecutive frames. Both collective and single cell velocity vectors were smoothed with a moving average filter of 3 frames with unity weighting in the temporal domain. RMS speed were calculated for each cell/seed using the instantaneous velocity vectors.

Multiphoton microscopy. In order to image cell nuclei within large spheroids, we adapted a technique known as CUBIC (Clear, Unobstructed Brain/Body Imaging Cocktails) which was originally developed to enable optical clearing and high-resolution imaging of murine organs [33]. Briefly, CUBIC employs hydrophilic reagents to remove lipids (the main source of scattering within tissues), while preserving fluorescent proteins. Following the original protocol by Susaki et al.[33], we prepared a mixture of 25% wt urea (Fisher Scientific, No. U15), 25% wt Quadrol (N,N,N′,N′-Tetrakis(2-hydroxypropyl)ethylenediamine, Sigma-Aldrich, No. 122262), 15% Triton X-100 (Sigma-Aldrich, No. T8787), and dH_2O. At regular intervals after embedding, spheroids were fixed overnight using cold 4% PFA (Fisher Scientific, No. AAJ19943K2), and washed out twice using 1x PBS. Samples were pretreated for 2 hours in 2 ml of ½ diluted CUBIC reagent (50% vol/vol dH_2O) and then immersed in 1 ml CUBIC reagent with 2 µM DAPI (Fisher Scientific, No. D1306) under gentle shaking at room temperature. The CUBIC reagent and DAPI were refreshed every two days and samples were cleared for up to 14 days prior to imaging. The 3D organization of optically cleared spheroids in collagen was imaged using a Bruker Ultima Investigator multiphoton microscope (MPM). The laser beam was focused onto the spheroids through a 16x water-immersion objective (Nikon, 0.8 N.A., 3 mm working distance) mounted in upright configuration. We used an excitation wavelength of 880 nm to image both invading spheroids and collagen. Two-photon excitation fluorescence (TPEF) from DAPI stained nuclei was collected through a bandpass filter centered at 550 nm with a bandwidth of 100 nm, while second harmonic generation (SHG) signal from the collagen matrix was collected through a bandpass filter centered at 440 nm with a bandwidth of 80 nm. Images were collected using 1024 × 1024 pixels at a resolution of 0.805 µm/pixel and a pixel dwell time of 10 µs. Stacks were acquired using 5 µm steps and a thickness (variable in the range 400-1000 µm) that was determined depending on the spheroid size and degree of invasion. Laser power and photomultiplier tube voltage were increased to maintain a nearly constant signal across the spheroid and interpolated linearly though the PraireView software during acquisition.

Cell shape characterization. We used a customized analysis procedure in MATLAB to characterize the cell shapes from both micro- and macro-spheroids. Steps in the analysis pipeline are illustrated in Supplementary Figure 2 and described below.

Nuclei identification. Nuclei centers were identified based on local intensity maxima from fluorescent image stacks (DAPI or GLP-NLS) with adaptations of previously published methods [70, 75]. In brief, images were preprocessed with MATLAB function *medfilt2* and *smoothn* to minimize background noise and smooth out intensity variation within each nucleus. To reduce noise, background intensity outside the spheroid were

removed by thresholding for the lowest 10% of signal intensities. Local intensity maxima were then identified from each 2D image slice, and a connected component analysis and a search radius of 5 μm in 3D was used to identify nuclei centers. Accuracy of nuclei identification of each spheroid was assessed via visual inspection of the overlay between identified nuclei positions with fluorescent nuclei image stacks (Supplementary Figure 2B). Further validation of this nuclei identification algorithm was carried out by comparing algorithm-identified cell counts with the manual counts obtained using a hemocytometer after spheroid dissociation via trypsinization. Validation was performed for macro-spheroids seeded at different sizes for both MCF-10A and MDA-MB-231 cells (Supplementary Figure 2G).

Spheroid boundary segmentation. Spheroid boundaries were identified from either bright-field microscopy (for micro-spheroids) or multiphoton SHG (for macro-spheroids) z-stacks. The spheroid boundary was identified in a two-step (coarse and fine) segmentation process, adapting previously published protocols [76, 77]. Image z-stacks were preprocessed with intermediate steps including *histogram equalization*, *wiener* (8×8 pixels) and *median* (5×5 pixels) filters to enhance image contrast. Initial coarse segmentation was performed using the watershed algorithm on the gradient image of the resulting image z-stacks, supplemented with nuclei position information. The fine segmentation step involved adaptive k-means clustering based on variation in pixel intensities in the output image from the coarse segmentation step. The number of clusters segmented was determined automatically based on the distance between new and existing cluster centers from the previous iteration. The final spheroid boundary was taken as the data cloud outline of the spheroid cluster that formed a connected region with the largest volume. Validation was done by visual inspection of the overlay between identified spheroid boundaries with the raw image z-stacks (Supplementary Figure 2C).

Bounded Voronoi Tessellation. Voronoi tessellation of the nuclei centers were based on the observation by Voigt and Weis [78], who have shown that the vertices of each Voronoi cell are solution to sets of linear inequalities indexed by their nuclei centers. Delaunay triangulation of the nuclei centers was used to identify the Voronoi neighbors for each cell. The spheroid boundary data cloud was then downsampled to 5% while maintaining the shape of the spheroid. The set of linear inequality for each cell was then constructed from the union between the perpendicular bisectors between edges connecting the cell and its Voronoi neighbor; and the spheroid boundary identified from segmentation. Some cell-free regions in the macro-spheroid core caused the Voronoi tessellation to give falsely large cell volumes that included these regions, a double thresholding was applied to discard these cells. Voronoi cells were discarded if cell volumes exceeded 3000 μm^3 or maximum distance of a cell to its immediate neighbors was in the top 5% of average maximum distance between all neighbors (Supplementary Figure 2F).

Collagen gel structure and mechanics. Acellular collagen gels were polymerized within cylindrical PDMS wells. Structural and mechanical characterizations were carried out by using previously published methods [79]. Briefly, high resolution multiphoton microscopy and analysis via CT-FIRE, and open source code for segmentation of collagen fibers [80], led to measurement of matrix porosity and fiber density. Uniaxial confined compression experiments and fitting of experimental data to a finite deformation model for biphasic mixtures, led to estimation of bulk material properties and fluid transport properties [81, 82]. Due to the nonlinear mechanical behavior of collagen [83], we report the elastic energy storage under 18% compression as a measure of material properties and the hydraulic permeability from Darcy's law as a measure of fluid transport properties. Further information can be found in the Supplementary Methods.

Agent-based modeling. We developed a computational model that represents a hybrid between vertex [30] and particle-based [57] approaches. On a 2D computational domain, 152 cells were generated by a Voronoi tessellation of points randomly seeded (with Poisson sampling) in a circular area to form a cellular collective. Individual cells within the cellular collective were endowed with a randomly oriented cell motility vector v_0, viscoelastic mechanical properties, and cell-cell interactions. Overall, the cellular collective was modelled as a confluent tissue, with no birth and death events, and was considered homogenous (in terms of cell properties such as adhesion and inherent motility). Collagen was represented as posts that are randomly distributed around the cell collective and was modeled as non-motile and rigid, and thus confining the cells. (Supplementary Methods). To capture all possible invasion patterns, the model was configured with gradual increase in the magnitude of the cell motility vector v_0 and the density of collagen particles, which were chosen as state variables, while keeping constant all other simulation parameters (Supplementary Table 1). To account for the random orientation of the motility vector and for the randomness in spatial configuration of collagen particles, we ran 10 simulations (n=10) for each pair of state variable configuration in the model, and used the averaged result to represent the cell collective behavior for that state variable combination. At the

end of each simulation, the mean distance of the outermost 5% cells from the cellular collective centroid was used to represent the overall invasive behavior of the cellular collective. This measure was then pooled from multiple simulations across the range of values varied for the two state variables, and generated a histogram distribution used to identify the threshold criteria that best identified the invasive phenotypes and material phases: outermost distances below the 34th percentile were labeled as solid-like, between the 34th and 64th percentiles were labeled as fluid-like, and above the 64th percentile were labeled as gas-like. Within the model, these different material phases indicated different spheroid behaviors: a solid-like behavior represents lack of invasion, a fluid-like behavior represents collective invasion, and a gas-like behavior represents single cell invasion. Mapping the material phases and invasion patterns for each state variable combinations resulted in the jamming phase diagram. Sensitivity analysis showed the choice of exact threshold criteria, within the examined range, did not significantly impact configuration of the resultant phase diagram (Supplementary Table 2). Additionally, mean cell shape (defined as $perimeter/\sqrt{area}$ for cells in 2D), for cells in the solid-like phase were smaller ($p<0.001$) than cells in the fluid-like phase. Further information can be found in the Supplementary Methods.

Statistical methods. All of the data was analyzed in MATLAB. Experimental data are presented as mean ± STD. One-tailed t-tests were used to assess differences between spatial regions (core vs periphery) and stages of evolution (early vs late) of the micro-spheroid. A one-way ANOVA was used to test differences due to collagen concentration in the macro-spheroid, and post-hoc pair-wise comparisons were performed using the Bonferroni correction. Unless otherwise stated, $p<0.05$ was considered statistically significant.

Maximum likelihood estimation (MLE): We fitted SI distributions to the *k-gamma distribution* using maximum likelihood estimation as described previously [31]. In brief, for a data set $\{x_i\} i = 1, \dots, \mathrm{N}$, the likehood function to fit is $L(k) = \prod_{i=1}^{N} PDF(x_i; k)$, where $\mathrm{PDF}(\boldsymbol{x}; k) = k^k x^{k-1} e^{-kx}/\Gamma(k)$ is the *k-gamma* probability density function. For our purposes, the SIs were shifted and normalized, and defined as $\boldsymbol{x} = (SI - SI_{min})/(\overline{SI} - SI_{min})$, with $SI_{min} = 5.413$ based on Merkel and Manning [29].

Data Availability. Data that support the figures in this paper and other findings reported in this study are available from the corresponding author upon request.

Box 1: Effective Temperature

The standard definition of temperature is well understood, but it is sometimes useful to define an 'effective temperature' that has a functional equivalence. For example, Edwards and Oakeshott [84] in a conceptual leap considered the physics governing a powder, which is representative of a wider class of an inanimate inert collective systems that includes sand piles, pastes, colloid suspensions, emulsions, foams, or slurries [85]. In such a collective system thermal fluctuations are insufficient to drive microstructural rearrangements. As a result the system tends to become trapped far from thermodynamic equilibrium [85]. Edwards and Oakeshott suggested that this class of collective systems might be understood in terms of the statistical mechanics of what have come to be called jammed packing. Their conjecture was as follows: Of the great many possible jammed packings into which such a collective system might become trapped, in the vicinity of a jamming transition all packings become equally likely. The Edwards conjecture was validated only recently [86]. In these inanimate inert systems, the place of energy, E, in thermal systems is then taken by local available volume, V. This assertion leads to the definition of an effective temperature, T_{eff}, based upon the statistics of volume variation in jammed packings. Specifically, if in thermal systems,

$$T = 1 / (\partial S / \partial E) \qquad dE = T\, dS$$

then in these granular athermal systems,

$$T_{eff} = 1 / (\partial S / \partial V) \qquad dV = T_{eff}\, dS$$

where S is the configurational entropy.

These notions of jammed packings, configurational entropy, and an effective temperature were subsequently extended to the living epithelial monolayer by Atia et al [31]. They showed that just as volume variation follows a *k-gamma* distribution and maximizes configurational entropy in the jammed collective inanimate system[32, 84], so too does cell shape variation in the jammed confluent cellular system, both *in vitro* and *in vivo* [31].

T_{eff} in tumor invasion dynamics: Using hard spheres in solution as a model system for jamming, one axis of the jamming phase diagram is typically given by k_BT/U where k_B is the Boltzmann constant, T is the thermodynamic temperature and U in interparticle attractive energy. This ratio is akin to an effective temperature in these systems. When temperature is higher or the particles are less attractive, the system tends to be less jammed and more fluid like. In our computational model system for tumor dynamics (Figure 5), we find a similar balance between cellular propulsion and cell adhesion. If adhesion is kept constant as propulsion increases, we find that the cellular collective fluidizes. Indeed, MDA-MB-231 cells are both less adhesive (smaller effective interparticle energy) and more propulsive (higher effective temperature) than MCF-10A cells [52]. In concert with that expectation, MDA-MB-231 cells fluidize in the same surrounding matrix more easily than do MCF-10A cells (Figures 2 and 3).

Box 2: Effective Confinement Pressure

A variety of physical forces act to confine and direct collective cellular behavior. For example, cells within the tumor experience compressive stress due to uncontrolled growth. Indeed, Jain and colleagues have shown that the tumor interior develops compressive stresses large enough to collapse the intra-tumor vasculature [26, 27]. Literature developed by us [21, 24, 87, 88] and others [36, 89, 90] shows that these compressive stresses can lead to systematic decreases of cell and nuclear volumes with increasing compressive stress. Additionally, within multicellular tumor models – and within the human tumor explant – nuclear volume varies appreciably and systematically both in space and time [21]. As such, changes in cell and nuclear volume are sensitive to the local microenvironment [24, 91-95], although whether or not they can serve as a remote pressure sensor, as some suggest [36], remains debatable. It is notable that across these different systems cell volume appears to change in close accord with the well-known Boyle van 't Hoff relationship [24, 36, 87, 89, 90]. These volume changes also appear to be associated with changing mechanical properties of the cell, with a strong increase in cell stiffness as cell volume decreases. From the Boyle van 't Hoff relationship, calculation of the bulk osmotic modulus, B, is straightforward [87]:

$$B = -V(\partial \Pi / \partial V) = Nk_BTV / (V-V_{min})^2$$

where Π is the osmotic pressure, N is the total number of osmolytes, k_B is the Boltzmann constant, T is the temperature, V is the volume, and V_{min} is the osmotically inactive volume.

For reasons that remain unclear, both cortical and cytoplasmic stiffness are orders of magnitude smaller but follow the same functional trend [24, 87]. As is described below, increasing cell stiffness may influence jamming behavior and as such understanding these forces remains critical.

P_{conf} in tumor invasion dynamics: In jamming behavior of colloids, micro-gels or many collective systems, both particle number density and particle stiffness play critical roles; higher number densities and stiffer particles tend to promote jamming [96].When these factors are held constant but collagen density is high, our computational model shows that the cellular collective can be either solid-like or fluid-like depending on propulsion (and therefore T_{eff} ; Box 1) but cell escape as a gas is not possible (Figure 5). However, when collagen density is lowered, the cellular collective can become gas-like (depending on T_{eff}), in which case cells escape readily. Changing collagen density in this computational model is akin to changing an effective confinement pressure, P_{conf} , in which case the matrix is imagined to comprise a vessel that acts to confine the jammed collective. In concert with these notions, experiments show that MDA-MB-231 cells are softer and exert greater propulsive forces than do MCF-10A cells [52, 53] and, as expected, escape more easily into an equivalent matrix (Figs. 3,4).

FIGURES

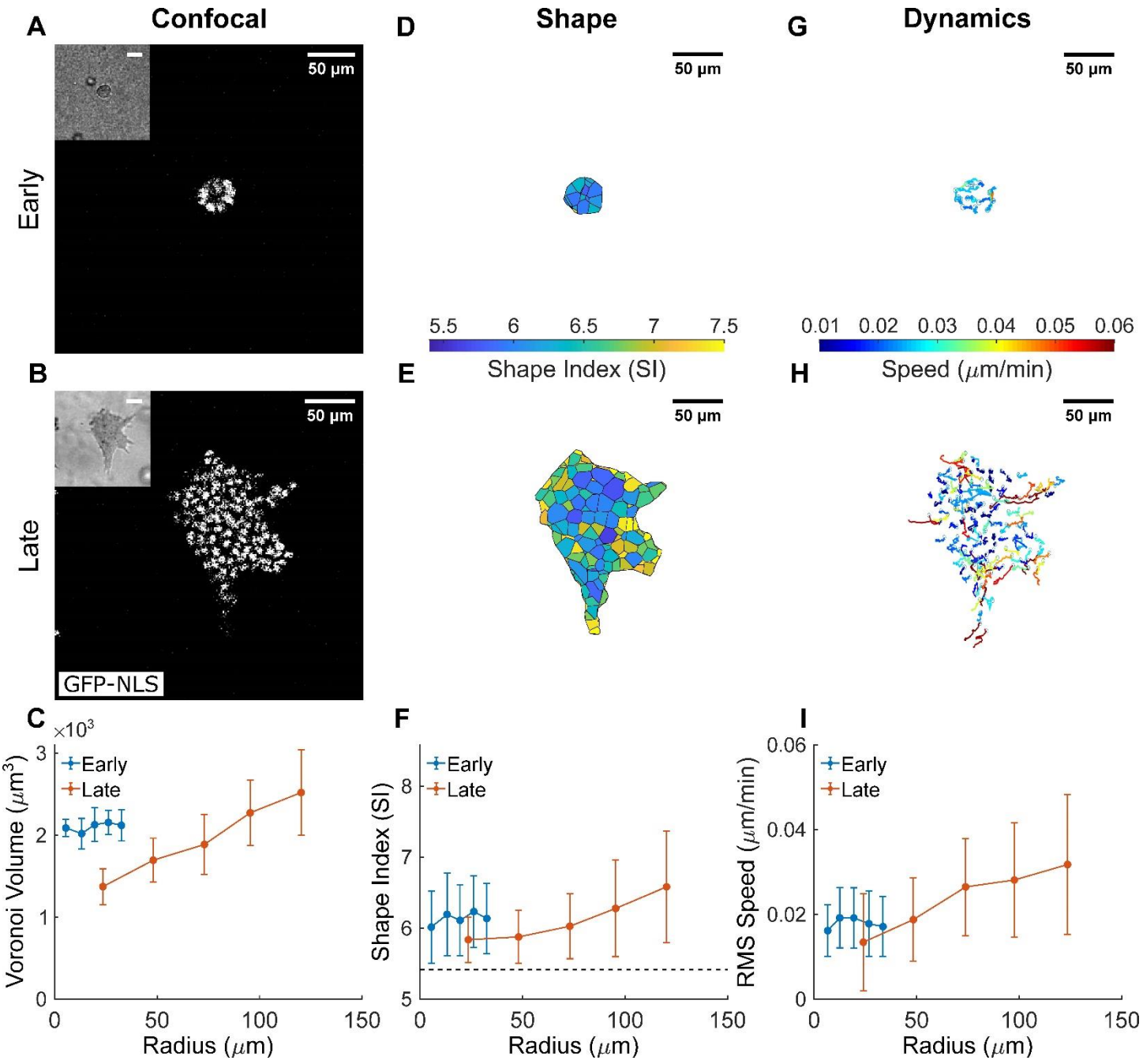

Figure 1. The MCF-10A micro-spheroid exhibits a jammed solid-like core and an unjammed fluid-like periphery. (A, B) Equatorial cross-sections of confocal microscopy images show cell nuclei distribution within micro-spheroids grown from GFP-NLS labelled MCF-10A cells at distinct stages of spheroid evolution: early stage (days 3-5; **A**) and late stage (days 7-10; **B**). Micro-spheroids at late stage are much larger compared to the early stage, and show clear invasive protrusions that extend into the ECM. Corresponding cross-sections of bright-field microscopy images outline the micro-spheroid boundary (inset), and are used to generate bounded Voronoi tessellation to estimate cell shape. (**C**) In late stage spheroids, but not early stage spheroids, cell volumes obtained by tessellation of nuclear centroids increase with increasing radial position. This result is

consistent with previous observations in this model system and attributed to an increase in intra-tumor compressive stress [21]. (**D, E**) The corresponding cell shapes are shown as 2D cross-sections, color-coded according to their respective 3D Shape Index (SI). Cell SIs exhibit more variability in the late, than early stage spheroid. (**F**) Compared to the early stage spheroid, cells in the late stage spheroid core have smaller average SI. In late stage, but not early stage, SI increased with increasing radial position within the spheroid. This is suggestive of the development of a jammed solid-like core and an unjammed fluid-like periphery. The horizontal dashed line indicates the SI threshold for solid to fluid transition, where proximity away from the threshold (SI > 5.4) suggests transition towards a more fluid-like phase [29]. (**G, H**) 2D projections of 3D nuclear trajectories tracked over 8 hours reveal that within the early stage spheroid cell migration is fairly homogenous, whereas in the late stage spheroid, migratory patterns become highly dynamic. Nuclear trajectories are color-coded according to average migratory speed of the cell over the observation window. (**I**) Compared to the homogenous cell dynamics in the early stage spheroid, cells in the late stage spheroid develop a positive radial gradient in migratory dynamics. Consequently, less motile cells are located in the jammed core while more motile cells are located in the unjammed periphery. Data for radial distributions are presented as mean ± STD (n = 5 for both early and late stage spheroids).

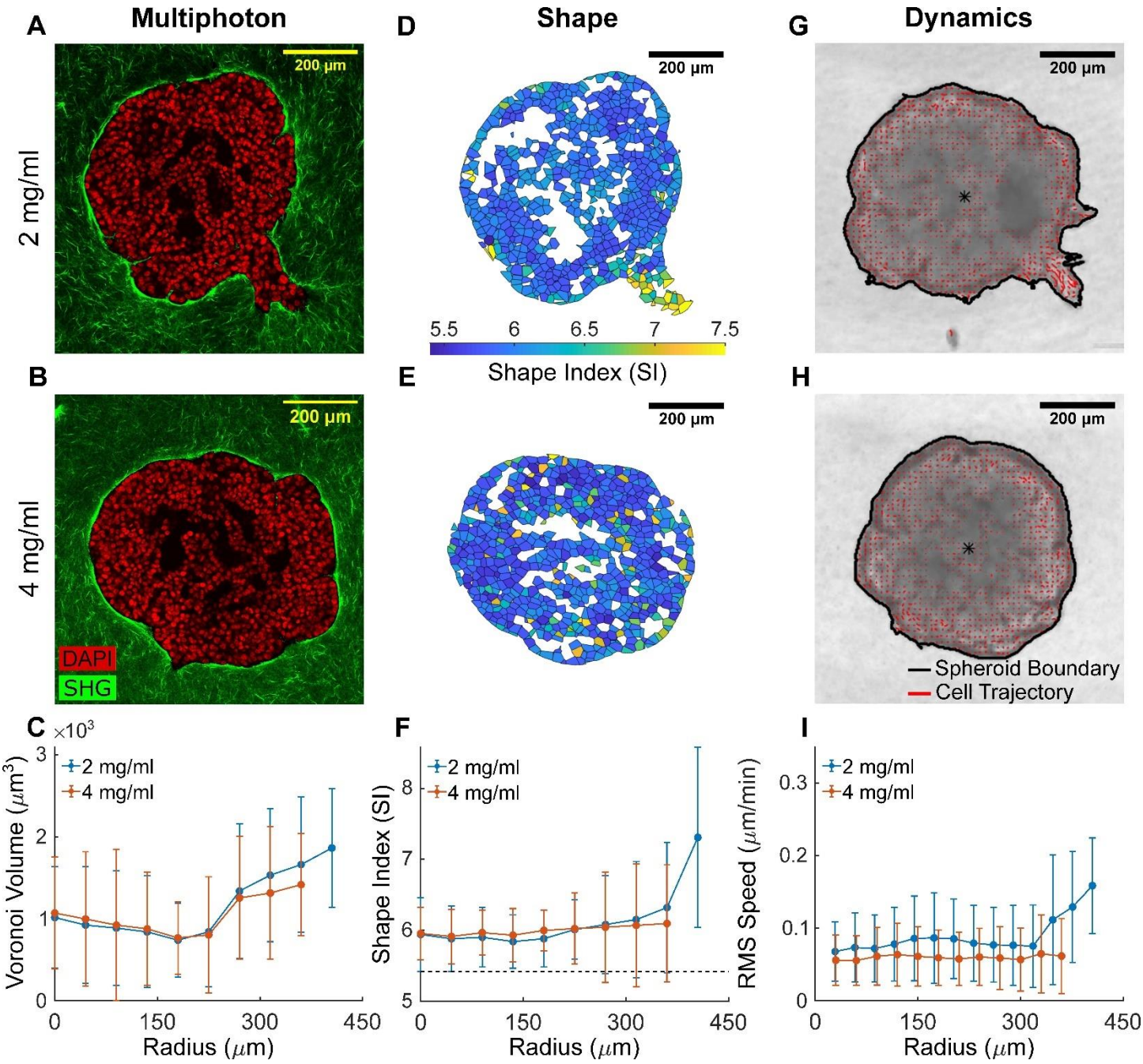

Figure 2. In a manner dependent on collagen concentration, MCF-10A macro-spheroid locally unjams and fluidizes at the periphery during collective invasion. (A, B) Representative equatorial cross-sections of multiphoton images show MCF-10A macro-spheroid behavior when embedded in either 2 (low density) or 4 mg/ml (high density) collagen, with DAPI-stained cell nuclei shown in red and collagen fibers from SHG shown in green. In low density collagen **(A)**, the spheroid develops collective invasive protrusions, while in high density collagen **(B)**, no invasion is observed. Cell-free voids (black) are due to Matrigel used to promote spheroid formation (Methods, Supplementary Figure 1); cells immediately neighboring this cell-free region are excluded from subsequent structural analysis (Methods, Supplementary Figure 2). (**C**) Similar to observations from the MCF-10A micro-spheroids, Voronoi cell volumes increased from the macro-spheroid core to the periphery. In contrast to the micro-spheroids, average cell volumes from macro-spheroids cultured at both

collagen densities are smaller, and suggest that cells in the macro-spheroid experience greater compressive stress (cf. Figure 1C). (**D-E**) The corresponding cell shapes are shown as 2D cross-sections, color-coded according to their respective 3D Shape Index (SI). Increased and more variable SIs are localized in the region of the spheroid periphery that undergoes collective invasion (**D**). On the other hand, SIs remain narrowly distributed, in the rest of the spheroid periphery and in the core regardless of collagen density. (**F**) In fact, SIs are homogeneously distributed near the threshold for solid-fluid transition (horizontal dashed line indicates solid-fluid transition point at SI=5.4 [29]). SIs increased only at the invasive protrusions suggest localized unjamming and fluidization is associated with invasion. (**G-H**) Representative DIC images are shown for MCF-10A macro-spheroids cultured in 2 and 4 mg/ml collagen, with cell migratory trajectories (from optical flow, Methods) superimposed in red. Longer trajectories are observed at the collectively invading regions (**G**). The spheroid boundaries are outlined in black. (**I**) Radial distributions of average cell migratory speed quantified for the final 8-hour observation window (40-48 hours) conform to expectations from cell shapes. In both collagen densities, migratory speed is homogenously low in the spheroid core, and increased only at sites of localized invasive protrusions. Data for radial distributions are presented as mean ± STD (n = 3 for both 2 and 4 mg/ml spheroids).

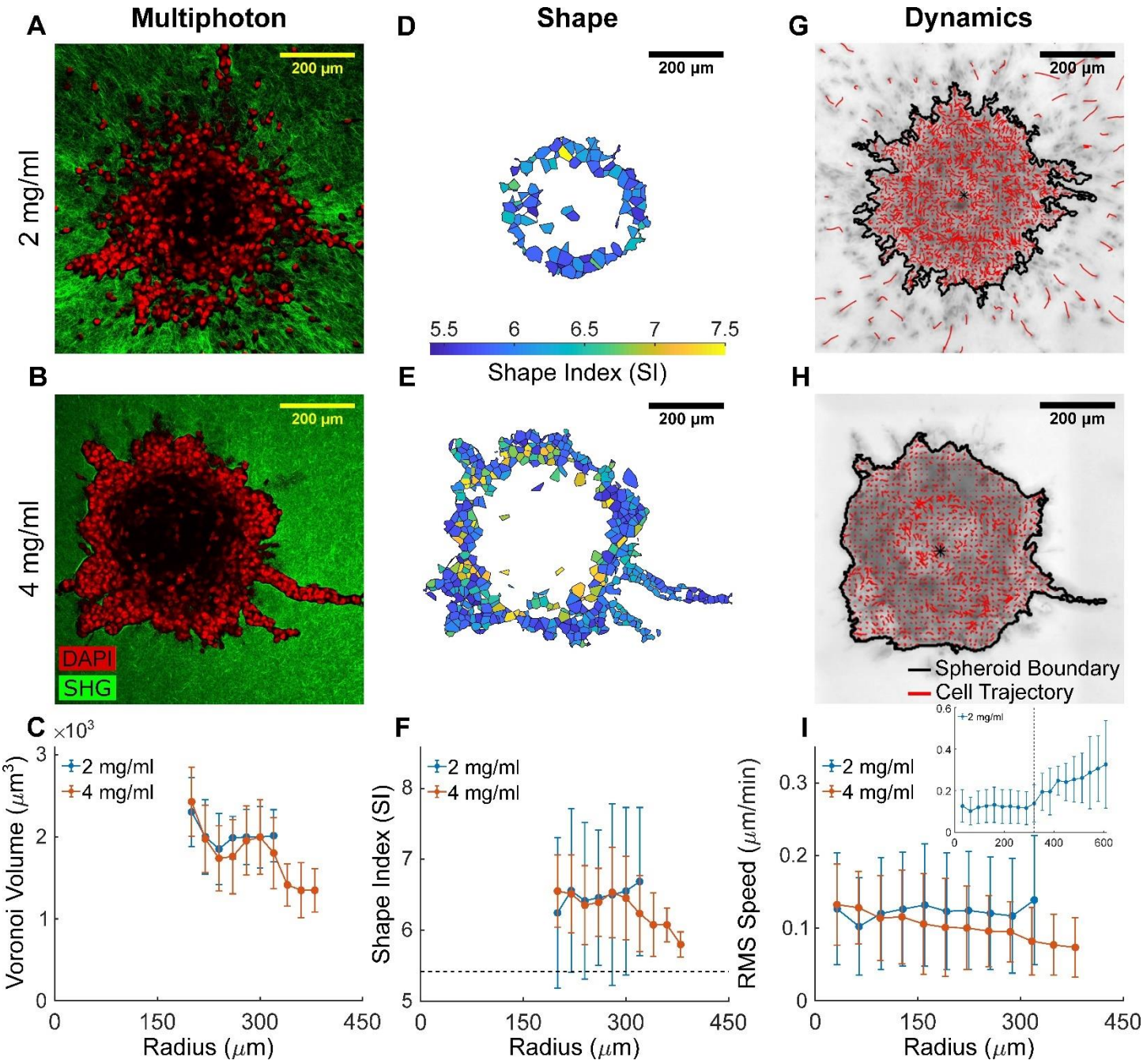

Figure 3. The metastatic MDA-MB-231 spheroid exhibits an unjammed fluid-like phase and undergoes drastically different patterns of invasion depending on collagen concentration. (**A, B**) Representative equatorial cross-sections of multiphoton images show MDA-MB-231 macro-spheroids exhibiting distinct invasion patterns when embedded in low density (2 mg/ml) versus high density (4 mg/ml) collagen. DAPI-stained cell nuclei are shown in red and collagen fibers from SHG are shown in green. In low density collagen **(A)**, these metastatic cells scatter from the spheroid core as individual, gas-like particles. Conversely, in high density collagen **(B)**, single-cell dominant scattering is subdued and invasion is in the form of collective, fluid-like protrusions. We note that the center of MDA-MB-231 spheroids is devoid of cells, as confirmed by staining of histological cross-sections (Supplementary Figure 1), and thus result in a hollow shell of highly motile cells

rather than a nearly solid spherical structure. Only cells that remain part of the collective are included in the structural analyses (Methods, Supplementary Figure 2), hence the absence of data for the first 200 μm of the associated radial distributions. (**C**) Average Voronoi volumes suggest that MDA-MB-231 cells have larger volumes with respect to their MCF-10A counterparts (cf. Figure 2C). In 2 mg/ml collagen, cell volumes remain roughly independent of radial position. In 4 mg/ml collagen, instead, cell volumes show a decreasing radial gradient. This decrease in cell volume from the spheroid core to the invasive protrusion suggests elevated stress in invading cells from confinement by the collagen matrix. (**D-E**) The corresponding cell shapes are shown as 2D cross-sections, color-coded according to their respective 3D Shape Index (SI). Regardless of collagen concentration, cells from MDA-MB-231 spheroids display higher SI with respect to MCF-10A spheroids (cf. Figure 2D-E) (**F**) Radial distribution of average SI values is consistent with an unjammed fluid-like phase (horizontal dashed line indicates solid-fluid transition point at SI=5.4 [29]). In high density collagen, a radially decreasing gradient in SI suggests that cells jam while invading collectively under matrix confinement. (**G-H**) Representative DIC images are shown for MDA-MB-231 macro-spheroids cultured in 2 and 4 mg/ml collagen, with cell migratory trajectories (from optical flow, Methods) superimposed in red. The spheroid boundaries are outlined in black. Cell dynamics mirrors structural signatures of cell jamming/unjamming. (**I**) Radial distributions of RMS speed quantified for the last 8-hour observation window (40-48 hours) show that cells in MDA-MB-231 macro-spheroids have homogeneously higher speeds with respect to MCF-10A spheroids (cf. Figure 2I) and are thus more fluid-like. In low density collagen, cell speed increases further as soon as cells detach from the spheroid and invade as single, gas-like particles (inset, where the radial position of the spheroid boundary is marked by a dashed vertical line). This observation supports the proposed analogy of fluid-to-gas transition. In high density collagen, RMS speed decrease radially with collective invasion, and is supportive of a fluid-to-solid transition due to confinement-induced jamming [13]. Data for radial distributions are presented as mean ± STD (n = 3 for both 2 and 4 mg/ml spheroids).

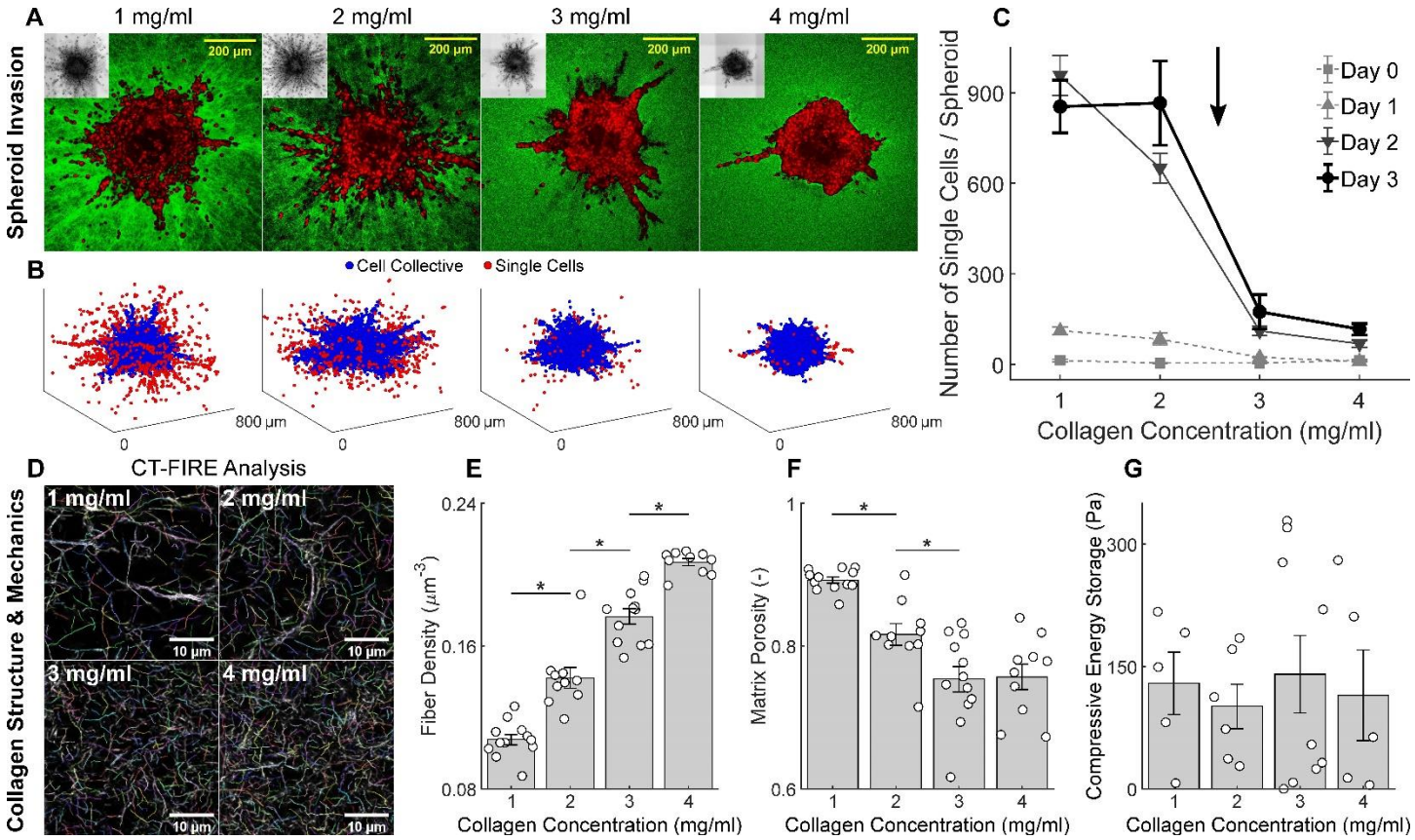

Figure 4. Collagen fiber density, not mechanics, modulates the critical switch in invasion phenotype observed in MDA-MB-231 spheroids. (**A**) Representative equatorial cross-sections of multiphoton images show MDA-MB-231 spheroids after 3 days of invasion in graded collagen concentrations (between 1 and 4 mg/ml) along with the associated DIC minimum intensity projections (insets). Single-cell migration is observed primarily in 1 and 2 mg/ml while collective migration is observed primarily in 3 and 4 mg/ml. (**B**) Corresponding 3D rendering of cell nuclei distributions identified from automated analysis of multiphoton image stacks (Methods). Nuclei are color-coded based on whether they remain within the cell collective (blue) or are detected as single cells (red). **(C)** Immediately after embedding in collagen (day 0), all cells are part of the multicellular collective with no invasion at any collagen density. As the spheroid evolves over time (days 1, 2 and 3), a striking gas-like phase and corresponding single cell escape progressively emerged at lower collagen concentrations (1 and 2 mg/ml) but not higher collagen concentrations (3 and 4 mg/ml). By day 3, a switch-like biphasic reduction in the number of single invading cells emerged when collagen concentration was increased from 2 to 3 mg/ml. The temporal evolution of single cell invasion as a function of collagen concentration supports the existence of criticality between 2 and 3 mg/ml, at which point the invasive phenotype switches abruptly from single to collective invasion. Single cell counting data are shown from days 0-1-2-3 and collagen concentrations of 1-2-3-4 mg/ml, n = 3 per group, except for day 0 - 1 mg/ml (n = 2) and day 2 - 2 mg/ml (n = 9). The significance of differences due to collagen concentration and time were quantified using a one-way ANOVA and post-hoc pairwise comparisons with Bonferroni correction. Statistical significance was achieved between 1 and 2 mg/ml at day 2 ($p < 0.05$), and between 2 and 3 mg/ml at days 1 ($p < 0.05$), 2 ($p < 0.01$), and

3 ($p < 0.01$), while no significant differences were observed between 3 and 4 mg/ml. The sharp and statistically significant transition between 2 and 3 mg/ml is therefore indicated with an arrow. We examined whether this transition is due to differences in collagen structure or mechanics. (**D**) High-resolution multiphoton images show representative acellular collagen networks at 1 to 4mg/ml, with individually segmented fibers from CT-FIRE analysis [80] as indicated by different colors. We quantified microstructural and mechanical properties of these collagen networks by combining multiphoton imaging and mechanical testing under confined compression (Methods and Supplementary Material). (**E**) Fiber density and (**F**) matrix porosity display clear trends with increasing collagen concentration between 1 and 4 mg/ml. (**G**) In contrast, compressive energy storage (under 18% compression), which quantifies nonlinear mechanical properties of the matrix, are indistinguishable between 1 and 4mg/ml. Therefore, collagen fiber density, rather than mechanics, represents a control variable for 3D cell jamming. Microstructural data are shown from 1 mg/ml (n = 12), 2 mg/ml (n = 10), 3 mg/ml (n = 12), and 4 mg/ml (n = 12) collagen gels. Mechanical data are shown from 1 mg/ml (n = 5), 2 mg/ml (n = 6), 3 mg/ml (n = 9), and 4 mg/ml (n = 5) collagen gels. * indicates statistical significance at $p < 0.05$.

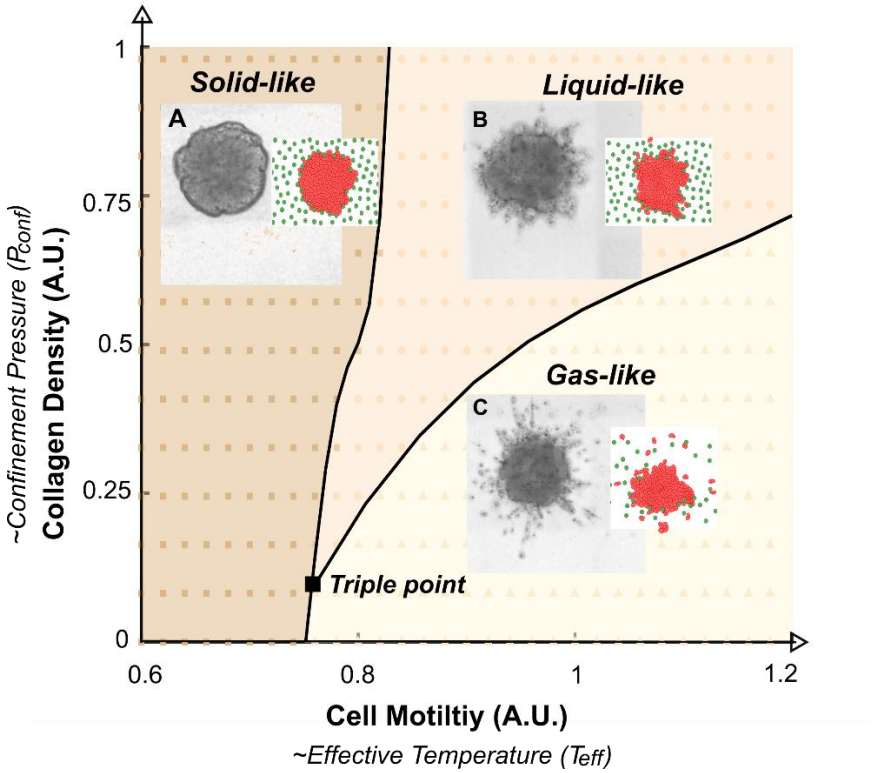

Figure 5. A 2D computational model of a multicellular cluster in collagen reveals that tumor invasion phenotypes and associated material states are governed by a jamming phase diagram. This phase diagram was generated by gradually incrementing two state variables: cell motility and collagen density, both expressed in arbitrary units (A.U.). Coexistence phase boundaries (black lines) were obtained as best-fit curves that separate data points belonging to different material phases. Near each phase boundary, the material phases become indistinguishable. Material phases of the simulated spheroid are determined based on mean distance of the outermost 5% cells from the spheroid (c.f. Supplementary Methods), and correspond to different spheroid behaviors: solid-like (squares), fluid-like (circles), and gas-like (triangles). Each data point represents the mean of n = 10 simulations, corresponding to the same set of state variables but different locally random configurations of collagen particles and motility vectors. By tuning only these two state variables, the model recapitulates much of the experimentally observed behaviors. For each material phase on the diagram, representative DIC images from experiments (left) are shown in comparison to representative snapshots at the end of model simulations (right). **(A)** In the solid-like phase, a MCF-10A macro-spheroid in high collagen density (4 mg/ml) is shown in comparison to simulation result parameterized with low cell motility (0.2) and high collagen density (0.82); **(B)** In the fluid-like phase: a MDA-MB-231 macro-spheroid in high collagen density (4 mg/ml) is shown in comparison to simulation result parameterized with high cell motility (1.0) and high collagen density (0.82); **(C)** In the gas-like phase, a MDA-MB-231 macro-spheroid in low collagen density (2 mg/ml) is shown in comparison to simulation result parameterized with high cell motility (1.0) and low collagen density (0.21). In the simulation snapshots, cells are represented as orange particles

and collagen is represented as green particles. Overall, we observe that at low cell motility, and thus low T_{eff} , the system is homogeneously “cold” and the spheroid shows a solid-like behavior regardless of collagen density(Box 1). However, at higher T_{eff} the collagen density, and hence P_{conf}, determines fluid-like or gas-like behaviors (Box 2).

Table 1: Across different spheroid systems, cell types, and experimental conditions, drastic changes in invasive phenotypes are reflected by transitions between material phases. Measured trends and observations are summarized relative to the early stage MCF-10A micro-spheroid. The two spheroid systems were labelled as "Micro" and "Macro" based on the approximate number of cells contained in the multicellular clusters. "Early Stage" and "Late Stage" conditions correspond to the early (day 3-5) and late (day 7-10) stages of evolution for MCF-10A micro-spheroid. "Low ECM Density" and "High ECM Density" correspond, respectively, to 2 and 4 mg/ml collagen concentration in which macro-spheroids were embedded. Spheroids were roughly grouped into core ("c") and periphery ("p") regions, to compare trends in the measured values (Shape Index, Motility, Cell Volume). Such trends and the associated radial gradients underlie the observation of different material phases and invasive modalities. *****Within MCF-10A macro-spheroids in 4 mg/ml collagen, there was a radial increase in cell volume but not SI and motility. The column "Reference" specifies the sections in the main text and the figure where these observations are reported and discussed in detail: [a] observations reported in section: *In the MCF-10A micro-spheroid, the core approaches a jammed, solid-like phase;* [b] observations reported in section: *In the MCF-10A macro-spheroid, the periphery invades as a locally unjammed fluid-like phase*; [c] observations reported in section*: In MDA-MB-231 macro-spheroids, the invasive phenotype switches at a critical ECM density*

Experimental Conditions			**Measured Trends**					**Observations**			**Reference**
Spheroid System	*Cell Type*	*Condition*	*Region*	*Shape Index*	*Motility*	*Cell Volume*	*Radial Gradient*	*Invasion*	*Invasive Modality*	*Material Phase*	
Micro n_{cells} ~ $O(10^1\text{-}10^2)$	MCF-10A	Early Stage	c	-	-	-	No	No	-	Fluid	Figure 1[a]
			p	-	-	-					
		Late Stage	c	↓	↓	↓	Yes	Yes	Collective	Solid → Fluid	
			p	↑	↑	↑					
Macro n_{cells} ~ $O(10^3\text{-}10^4)$	MCF-10A	Low ECM Density	c	-	-	-	Yes	Yes	Collective	Solid → Fluid	Figure 2[b]
			p	↑	↑	↑					
		High ECM Density	c	-	-	-	No*	No	-	Solid	
			p	-	-	↑					
	MDA-MB-231	Low ECM Density	c	↑↑	↑↑	↑	No	Yes	Single Cell	Fluid → Gas	Figures 3,4[c]
			p	↑↑	↑↑	↑					
		High ECM Density	c	↑↑	↑↑	↑	Yes	Yes	Collective	Fluid → Solid	
			p	↓	↓	↓					

REFERENCES

1. Lautscham, L.A., et al., *Migration in confined 3D environments is determined by a combination of adhesiveness, nuclear volume, contractility, and cell stiffness.* Biophysical journal, 2015. **109**(5): p. 900-913.
2. Friedl, P. and K. Wolf, *Tumour-cell invasion and migration: diversity and escape mechanisms.* Nature reviews cancer, 2003. **3**(5): p. 362.
3. Friedl, P., et al., *Classifying collective cancer cell invasion.* Nature cell biology, 2012. **14**(8): p. 777-783.
4. Waclaw, B., et al., *A spatial model predicts that dispersal and cell turnover limit intratumour heterogeneity.* Nature, 2015. **525**(7568): p. 261-264.
5. Ghajar, C.M. and M.J. Bissell, *Metastasis: pathways of parallel progression.* Nature, 2016. **540**(7634): p. 528-529.
6. Zhang, Y. and R.A. Weinberg, *Epithelial-to-mesenchymal transition in cancer: complexity and opportunities.* Frontiers of medicine, 2018. **12**(4): p. 361-373.
7. Thiery, J.P., et al., *Epithelial-mesenchymal transitions in development and disease.* cell, 2009. **139**(5): p. 871-890.
8. Hosseini, H., et al., *Early dissemination seeds metastasis in breast cancer.* Nature, 2016. **540**(7634): p. 552-558.
9. Klein, C.A., *Parallel progression of primary tumours and metastases.* Nature Reviews Cancer, 2009. **9**(4): p. 302-312.
10. Clark, A.G. and D.M. Vignjevic, *Modes of cancer cell invasion and the role of the microenvironment.* Curr Opin Cell Biol, 2015. **36**: p. 13-22.
11. Friedl, P. and D. Gilmour, *Collective cell migration in morphogenesis, regeneration and cancer.* Nature reviews Molecular cell biology, 2009. **10**(7): p. 445.
12. Khalil, A.A., et al., *Collective invasion in ductal and lobular breast cancer associates with distant metastasis.* Clin Exp Metastasis, 2017. **34**(6-7): p. 421-429.
13. Haeger, A., et al., *Cell jamming: collective invasion of mesenchymal tumor cells imposed by tissue confinement.* Biochimica et Biophysica Acta (BBA)-General Subjects, 2014. **1840**(8): p. 2386-2395.
14. Oswald, L., et al., *Jamming transitions in cancer.* J Phys D Appl Phys, 2017. **50**(48): p. 483001.
15. Palamidessi, A., et al., *Unjamming overcomes kinetic and proliferation arrest in terminally differentiated cells and promotes collective motility of carcinoma.* Nature materials, 2019: p. 1-12.
16. Valencia, A.M.J., et al., *Collective cancer cell invasion induced by coordinated contractile stresses.* Oncotarget, 2015. **6**(41): p. 43438.
17. Angelini, T.E., et al., *Glass-like dynamics of collective cell migration.* Proc Natl Acad Sci U S A, 2011. **108**(12): p. 4714-9.
18. Tambe, D.T., et al., *Collective cell guidance by cooperative intercellular forces.* Nat Mater, 2011. **10**(6): p. 469-75.
19. Park, J.A., et al., *Unjamming and cell shape in the asthmatic airway epithelium.* Nat Mater, 2015. **14**(10): p. 1040-8.
20. Nnetu, K.D., et al., *The impact of jamming on boundaries of collectively moving weak-interacting cells.* New Journal of Physics, 2012. **14**(11): p. 115012.
21. Han, Y.L., et al., *Cell swelling, softening and invasion in a three-dimensional breast cancer model.* Nature Physics, 2020. **16**(1): p. 101-108.
22. Chaudhuri, O., et al., *Extracellular matrix stiffness and composition jointly regulate the induction of malignant phenotypes in mammary epithelium.* Nat Mater, 2014. **13**(10): p. 970-8.
23. Spatarelu, C.-P., et al., *Biomechanics of Collective Cell Migration in Cancer Progression: Experimental and Computational Methods.* ACS Biomaterials Science & Engineering, 2019. **5**(8): p. 3766-3787.
24. Guo, M., et al., *Cell volume change through water efflux impacts cell stiffness and stem cell fate.* Proceedings of the National Academy of Sciences, 2017. **114**(41): p. E8618-E8627.
25. Jovtchev, G., et al., *Nuclear DNA content and nuclear and cell volume are positively correlated in angiosperms.* Cytogenetic and genome research, 2006. **114**(1): p. 77-82.
26. Stylianopoulos, T., et al., *Coevolution of solid stress and interstitial fluid pressure in tumors during progression: implications for vascular collapse.* Cancer Res, 2013. **73**(13): p. 3833-41.
27. Tse, J.M., et al., *Mechanical compression drives cancer cells toward invasive phenotype.* Proc Natl Acad Sci U S A, 2012. **109**(3): p. 911-6.
28. Bi, D., et al., *Energy barriers and cell migration in densely packed tissues.* Soft Matter, 2014. **10**(12): p. 1885-90.

29. Merkel, M. and M.L. Manning, *A geometrically controlled rigidity transition in a model for confluent 3D tissues.* New Journal of Physics, 2018. **20**(2): p. 022002.
30. Bi, D., et al., *Motility-driven glass and jamming transitions in biological tissues.* Phys Rev X, 2016. **6**(2).
31. Atia, L., et al., *Geometric constraints during epithelial jamming.* Nat Phys, 2018. **14**: p. 613-620.
32. Aste, T. and T. Di Matteo, *Emergence of Gamma distributions in granular materials and packing models.* Phys Rev E Stat Nonlin Soft Matter Phys, 2008. **77**(2 Pt 1): p. 021309.
33. Susaki, E.A., et al., *Advanced CUBIC protocols for whole-brain and whole-body clearing and imaging.* Nature protocols, 2015. **10**(11): p. 1709.
34. Karrobi, K., et al., *Diffuse and nonlinear imaging of multiscale vascular parameters for in vivo monitoring of preclinical mammary tumors.* Journal of biophotonics, 2019. **12**(6): p. e201800379.
35. Vig, D.K., A.E. Hamby, and C.W. Wolgemuth, *On the quantification of cellular velocity fields.* Biophysical journal, 2016. **110**(7): p. 1469-1475.
36. Khavari, A. and A.J. Ehrlicher, *Nuclei deformation reveals pressure distributions in 3D cell clusters.* PloS one, 2019. **14**(9).
37. Ranft, J., et al., *Fluidization of tissues by cell division and apoptosis.* Proc Natl Acad Sci U S A, 2010. **107**(49): p. 20863-8.
38. Devany, J., et al., *Cell division Rate Controls Cell Shape Remodeling in Epithelia.* BioRxiv, 2019: p. 804294.
39. Czajkowski, M., et al., *Glassy dynamics in models of confluent tissue with mitosis and apoptosis.* Soft matter, 2019. **15**(44): p. 9133-9149.
40. Matoz-Fernandez, D., et al., *Cell division and death inhibit glassy behaviour of confluent tissues.* Soft matter, 2017. **13**(17): p. 3205-3212.
41. Malmi-Kakkada, A.N., et al., *Cell Growth Rate Dictates the Onset of Glass to Fluidlike Transition and Long Time Superdiffusion in an Evolving Cell Colony.* Physical Review X, 2018. **8**(2).
42. Sinha, S., et al., *Spatially heterogeneous dynamics of cells in a growing tumor spheroid: Comparison between Theory and Experiments.* arXiv preprint arXiv:1911.06383, 2019.
43. Klank, R.L., S.S. Rosenfeld, and D.J. Odde, *A Brownian dynamics tumor progression simulator with application to glioblastoma.* Converg Sci Phys Oncol, 2018. **4**(1).
44. Cailleau, R., et al., *Tissue culture studies on pleural effusions from breast carcinoma patients.* Cancer research, 1974. **34**(4): p. 801-809.
45. Prat, A., et al., *Phenotypic and molecular characterization of the claudin-low intrinsic subtype of breast cancer.* Breast cancer research, 2010. **12**(5): p. R68.
46. Dent, R., et al., *Triple-negative breast cancer: clinical features and patterns of recurrence.* Clin Cancer Res, 2007. **13**(15 Pt 1): p. 4429-34.
47. Lehmann, B.D., et al., *Identification of human triple-negative breast cancer subtypes and preclinical models for selection of targeted therapies.* The Journal of clinical investigation, 2011. **121**(7): p. 2750-2767.
48. Neve, R.M., et al., *A collection of breast cancer cell lines for the study of functionally distinct cancer subtypes.* Cancer cell, 2006. **10**(6): p. 515-527.
49. Kluger, H.M., et al., *Using a xenograft model of human breast cancer metastasis to find genes associated with clinically aggressive disease.* Cancer research, 2005. **65**(13): p. 5578-5587.
50. Ivascu, A. and M. Kubbies, *Diversity of cell-mediated adhesions in breast cancer spheroids.* International journal of oncology, 2007. **31**(6): p. 1403-1413.
51. Ivascu, A. and M. Kubbies, *Rapid generation of single-tumor spheroids for high-throughput cell function and toxicity analysis.* Journal of biomolecular screening, 2006. **11**(8): p. 922-932.
52. Kim, J.H., et al., *Unjamming and collective migration in MCF10A breast cancer cell lines.* Biochemical and biophysical research communications, 2020. **521**(3): p. 706-715.
53. Kraning-Rush, C.M., J.P. Califano, and C.A. Reinhart-King, *Cellular traction stresses increase with increasing metastatic potential.* PloS one, 2012. **7**(2).
54. Raman, P.S., et al., *Probing cell traction forces in confined microenvironments.* Lab on a Chip, 2013. **13**(23): p. 4599-4607.
55. Steinwachs, J., et al., *Three-dimensional force microscopy of cells in biopolymer networks.* Nature methods, 2016. **13**(2): p. 171.

56. Duval, K., et al., *Modeling physiological events in 2D vs. 3D cell culture.* Physiology, 2017. **32**(4): p. 266-277.
57. Boromand, A., et al., *Jamming of Deformable Polygons.* Phys Rev Lett, 2018. **121**(24): p. 248003.
58. Parisi, G. and F. Zamponi, *Mean-field theory of hard sphere glasses and jamming.* Reviews of Modern Physics, 2010. **82**(1): p. 789-845.
59. Berthier, L., E. Flenner, and G. Szamel, *Glassy dynamics in dense systems of active particles.* The Journal of chemical physics, 2019. **150**(20): p. 200901.
60. Fredberg, J.J., *Power steering, power brakes, and jamming: Evolution of collective cell-cell interactions*. 2014, American Physiological Society Bethesda, MD.
61. Guo, M., et al., *Probing the Stochastic, Motor-Driven Properties of the Cytoplasm Using Force Spectrum Microscopy.* Cell, 2014. **158**(4): p. 822-832.
62. Nia, H.T., et al., *Solid stress and elastic energy as measures of tumour mechanopathology.* Nature biomedical engineering, 2016. **1**(1): p. 1-11.
63. Meng, F. and G. Wu, *The rejuvenated scenario of epithelial–mesenchymal transition (EMT) and cancer metastasis.* Cancer and Metastasis Reviews, 2012. **31**(3-4): p. 455-467.
64. Brabletz, T., et al., *EMT in cancer.* Nature Reviews Cancer, 2018. **18**(2): p. 128.
65. Mitchel, J.A., et al., *The unjamming transition is distinct from the epithelial-to-mesenchymal transition.* bioRxiv, 2019: p. 665018.
66. Denais, C.M., et al., *Nuclear envelope rupture and repair during cancer cell migration.* Science, 2016. **352**(6283): p. 353-358.
67. Pfeifer, C.R., et al., *Genome variation across cancers scales with tissue stiffness - an invasion-mutation mechanism and implications for immune cell infiltration.* Curr Opin Syst Biol, 2017. **2**: p. 103-114.
68. Sung, K.E., et al., *Control of 3-dimensional collagen matrix polymerization for reproducible human mammary fibroblast cell culture in microfluidic devices.* Biomaterials, 2009. **30**(27): p. 4833-4841.
69. Harjanto, D., J.S. Maffei, and M.H. Zaman, *Quantitative analysis of the effect of cancer invasiveness and collagen concentration on 3D matrix remodeling.* PloS one, 2011. **6**(9).
70. Crocker, J.C. and D.G. Grier, *Methods of digital video microscopy for colloidal studies.* Journal of colloid and interface science, 1996. **179**(1): p. 298-310.
71. Preibisch, S., S. Saalfeld, and P. Tomancak, *Globally optimal stitching of tiled 3D microscopic image acquisitions.* Bioinformatics, 2009. **25**(11): p. 1463-5.
72. Guizar-Sicairos, M., S.T. Thurman, and J.R. Fienup, *Efficient subpixel image registration algorithms.* Opt Lett, 2008. **33**(2): p. 156-8.
73. Otsu, N., *A threshold selection method from gray-level histograms.* IEEE transactions on systems, man, and cybernetics, 1979. **9**(1): p. 62-66.
74. Farnebäck, G. *Two-frame motion estimation based on polynomial expansion*. in *Scandinavian conference on Image analysis*. 2003. Springer.
75. Toyoshima, Y., et al., *Accurate Automatic Detection of Densely Distributed Cell Nuclei in 3D Space.* PLoS Comput Biol, 2016. **12**(6): p. e1004970.
76. Tse, S., et al. *A combined watershed and level set method for segmentation of brightfield cell images*. in *Medical Imaging 2009: Image Processing*. 2009. International Society for Optics and Photonics.
77. Bradbury, L. and J.W. Wan, *A spectral k-means approach to bright-field cell image segmentation.* Conf Proc IEEE Eng Med Biol Soc, 2010. **2010**: p. 4748-51.
78. Voigt, I. and S. Weis, *Polyhedral Voronoi cells.* arXiv preprint arXiv:1003.4173, 2010.
79. Ferruzzi, J., et al., *compressive Remodeling Alters fluid transport properties of collagen networks–implications for tumor Growth.* Scientific reports, 2019. **9**(1): p. 1-16.
80. Bredfeldt, J.S., et al., *Computational segmentation of collagen fibers from second-harmonic generation images of breast cancer.* J Biomed Opt, 2014. **19**(1): p. 16007.
81. Holmes, M.H., *Finite deformation of soft tissue: analysis of a mixture model in uni-axial compression.* J Biomech Eng, 1986. **108**(4): p. 372-81.
82. Ateshian, G.A., et al., *Finite deformation biphasic material properties of bovine articular cartilage from confined compression experiments.* J Biomech, 1997. **30**(11-12): p. 1157-64.

83. Han, Y.L., et al., *Cell contraction induces long-ranged stress stiffening in the extracellular matrix.* Proceedings of the National Academy of Sciences, 2018. **115**(16): p. 4075-4080.
84. Edwards, S.F. and R. Oakeshott, *Theory of powders.* Physica A: Statistical Mechanics and its Applications, 1989. **157**(3): p. 1080-1090.
85. Sollich, P., *Rheological constitutive equation for a model of soft glassy materials.* Physical Review E, 1998. **58**(1): p. 738.
86. Martiniani, S., et al., *Numerical test of the Edwards conjecture shows that all packings are equally probable at jamming.* Nature Physics, 2017. **13**(9): p. 848-851.
87. Zhou, E., et al., *Universal behavior of the osmotically compressed cell and its analogy to the colloidal glass transition.* Proceedings of the National Academy of Sciences, 2009. **106**(26): p. 10632-10637.
88. Li, Y., et al., *Compression-induced dedifferentiation of adipocytes promotes tumor progression.* Sci Adv, 2020. **6**(4): p. eaax5611.
89. Finan, J.D., et al., *Nonlinear osmotic properties of the cell nucleus.* Annals of biomedical engineering, 2009. **37**(3): p. 477.
90. Guilak, F., G.R. Erickson, and H.P. Ting-Beall, *The effects of osmotic stress on the viscoelastic and physical properties of articular chondrocytes.* Biophysical journal, 2002. **82**(2): p. 720-727.
91. Dahl, K.N., et al., *Power-law rheology of isolated nuclei with deformation mapping of nuclear substructures.* Biophysical journal, 2005. **89**(4): p. 2855-2864.
92. Pajerowski, J.D., et al., *Physical plasticity of the nucleus in stem cell differentiation.* Proceedings of the National Academy of Sciences, 2007. **104**(40): p. 15619-15624.
93. Discher, D.E., D.J. Mooney, and P.W. Zandstra, *Growth factors, matrices, and forces combine and control stem cells.* Science, 2009. **324**(5935): p. 1673-1677.
94. Swift, J., et al., *Nuclear lamin-A scales with tissue stiffness and enhances matrix-directed differentiation.* Science, 2013. **341**(6149): p. 1240104.
95. Sosale, N.G., et al., *Cell rigidity and shape override CD47's "self"-signaling in phagocytosis by hyperactivating myosin-II.* Blood, 2015. **125**(3): p. 542-52.
96. Liu, A.J. and S.R. Nagel, *Nonlinear dynamics: Jamming is not just cool any more.* Nature, 1998. **396**(6706): p. 21.